Geophysical Research Letters

Key Points:

- Atmospheric Rivers (ARs) experience upward latent heat flux (LHF) over the coastal ocean, strongest 1–3 days before and after landfall
- In El Niño winters, LHF during ARs is enhanced along the southern coast and reduced along the northern coast by ~70% relative to La Niña
- LHF decomposition reveals sea surface temperature variability via ENSO as a dominant contributor to interannual coastal LHF variations

Supporting Information:

- Supporting Information S1

Correspondence to:
S. T. Bartusek,
samueltb@princeton.edu

The Role of Nearshore Air-Sea Interactions for Landfalling Atmospheric Rivers on the U.S. West Coast

Samuel T. Bartusek[1,2] , **Hyodae Seo[2]** , **Caroline C. Ummenhofer[2]** , **and John Steffen[2]**

[1]Department of Geosciences, Princeton University, Princeton, NJ, US, [2]Department of Physical Oceanography, Woods Hole Oceanographic Institution, Woods Hole, MA, US

Abstract   Research on Atmospheric Rivers (ARs) has focused primarily on AR (thermo)dynamics and hydrological impacts over land. However, the evolution and potential role of nearshore air-sea fluxes during landfalling ARs are not well documented. Here, we examine synoptic evolutions of nearshore latent heat flux (LHF) during strong late-winter landfalling ARs (1979–2017) using 138 overshelf buoys along the U. S. west coast. Composite evolutions show that ARs typically receive upward (absolute) LHF from the coastal ocean. LHF is small during landfall due to weak air-sea humidity gradients but is strongest (30–50 W/m^2 along the coast) 1–3 days before/after landfall. During El Niño winters, southern-coastal LHF strengthens, coincident with stronger ARs. A decomposition of LHF reveals that sea surface temperature (SST) anomalies modulated by the El Niño Southern Oscillation dominate interannual LHF variations under ARs, suggesting a potential role for nearshore SST and LHF influencing the intensity of landfalling ARs.

Plain Language Summary   Atmospheric Rivers (ARs) are elongated streams of enhanced water vapor transport, contributing to a substantial fraction of total wintertime precipitation and extreme streamflow events along the U.S. west coast. Thus, better understanding the processes contributing to the intensity of landfalling ARs is of broad scientific and societal interests. Considerable efforts have been directed at their meteorological structures and hydrological impacts over land, but it remains unclear if and how the severity of landfalling ARs is influenced by their interactions with coastal oceans. Here, we use in situ near-surface atmospheric and sea surface temperature measurements from 138 overshelf buoys along the U.S. west coast to characterize variations of latent heat flux during strong late-winter landfalling ARs from 1979 to 2017. We find that the coastal ocean is an important heat and moisture source for ARs in the days before landfall. During El Niño events, the oceanic heat and moisture input to the atmosphere increases along the southern coast, coincident with more intense ARs. Further analysis shows that surface ocean temperature anomalies related to El Niño Southern Oscillation dominantly affect latent heat flux during landfalling ARs. Our results suggest a potential role for the coastal ocean in influencing the intensity of landfalling ARs.

1. Introduction

Atmospheric Rivers (ARs) are elongated and filamentary (typically >2,000 km long, <1,000 km wide) plumes of enhanced atmospheric water vapor content and transport, extending from the tropics toward the midlatitudes (e.g., Lavers et al., 2011; Neiman et al., 2008; Ralph et al., 2004; Zhu & Newell, 1998). Despite their small spatial footprint and short lifetime (Ralph et al., 2004, 2013), ARs achieve >90% of poleward moisture flux in the extratropics (Zhu & Newell, 1998) due to their high vapor transport. ARs play a vital role in the global hydrological cycle (e.g., Algarra et al., 2020).

ARs are particularly critical to hydroclimate variability and the water cycle in the western U.S. ARs deliver up to half of the water-year's precipitation and regional water resources (Dettinger et al., 2011; Gershunov et al., 2017; Guan et al., 2010) and have helped alleviate or terminate 30%–70% of the region's dry spells and droughts (Dettinger, 2013; Moore et al., 2012). However, the region is also vulnerable to hazards from ARs' intense precipitation. Nearly all extreme streamflow events and flooding are associated with ARs (Dettinger et al., 2011, 2012; Leung & Qian, 2009; Ralph et al, 2005, 2006, 2011; Ralph & Dettinger, 2012; Rutz et al., 2014; Smith et al., 2010; White et al., 2012). Therefore, better understanding the processes contributing
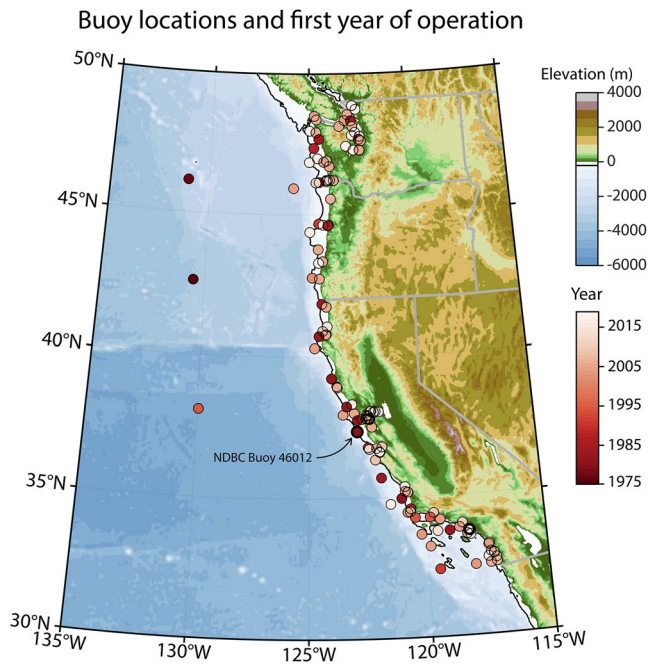
Buoy locations and first year of operation

Figure 1. Locations of 138 buoys used in the analysis, color-coded by their first year of measurements, are overlaid on topography and bathymetry. Most buoys are moored over the continental shelf, typically within the 200 m isobath (black curve). NDBC buoy 46012 (examined in Figure 4) is indicated. NDBC, National Data Buoyancy Center.

to the intensity of landfalling ARs is of broad scientific and economic interests (Corringham et al., 2019; Ralph et al., 2019a).

Despite extensive research into atmospheric dynamics (e.g., Payne & Magnusdottir, 2014; Zhang et al., 2019) and hydrological impacts (e.g., Neiman et al., 2011; Ralph et al., 2006) of ARs, the behavior of near-shore air-sea fluxes during landfalling ARs remains not well understood. As ARs approach the west coast, they traverse the coastal ocean, where substantial coastally trapped variability in upper ocean heat content and sea surface temperature (SST) influence the magnitude of air-sea fluxes on subseasonal to interannual time-scales. For example, a sustained network of glider observations (e.g., Todd et al., 2011) revealed substantial (±3–4ºC) nearshore SST and heat content anomalies along the U.S. west coast associated with the El Niño Southern Oscillation (ENSO). Persson et al. (2005) provided a case study of a landfalling AR resulting in widespread flooding in southern California in the winter of 1998, a strong El Niño year, in which localized deep convection was ascribed to enhanced latent heat flux (LHF) over this anomalously high SST. Furthermore, Gonzales et al. (2019) find that coastal SSTs influence AR landfall temperatures more strongly than along-track SSTs, and Chen and Leung (2020) provided modeling evidence that local SST warming significantly enhances AR intensity and precipitation, likely by increasing boundary layer instability and convective available potential energy (CAPE). However, it remains an open question whether enhanced SST variability in the coastal oceans associated with ENSO systematically influences air-sea moisture flux under landfalling ARs.

Here, we provide in situ information about synoptic LHF evolution during strong late-winter ARs (1979–2017) landfalling along the U.S. west coast. Given the strong impact of ENSO on west coast SST and precipitation (Jong et al., 2016), we further investigate the ENSO-related variability of LHF, its constituent variables via flux decomposition, and AR intensity.

ARs generally represent a nearly saturated air-mass over the cooler coastal waters, incurring reduced moisture exchanges as they approach the shore. This was demonstrated by Shinoda et al. (2019), who constructed composite AR evolutions based on the 1°-resolution OAFLUX data set (Yu et al., 2007), finding strong LHF anomalies upstream (far offshore) becoming small downstream (nearshore). Noting the transient nature of ARs and narrow spatial extent of the coastal shelf, in addition to challenges in satellite remote sensing of coastal meteorology and air-sea fluxes (Cronin et al., 2019), however, analysis is necessary based on in situ measurements that are designed for monitoring coastal processes to reinforce their finding. The authors also concluded that strong ARs typically correspond with negative heat flux anomaly near the coast. As we will show, despite this negative LHF anomaly, the absolute magnitude of LHF remains positive, indicating that the coastal ocean provides moisture and heat to ARs, potentially affecting their intensity.

2. Data and Methods

2.1. Datasets and Landfalling AR Index

Our in situ data set includes 138 overshelf buoys throughout the U.S. west coast (32–49ºN) operated by NOAA's National Data Buoy Center (NDBC), Integrated Ocean Observing System partners, and the National Ocean Service. Generally, these buoys are moored over the continental shelf and constitute a spatially (alongshore) dense array of long-term (1975–present) measurements of critical boundary layer parameters, including air temperature, humidity (albeit only at a few buoys), surface pressure, and wind speed at the subhourly sampling rate. These measurements are averaged at hourly intervals to ensure consistency across the buoys. Figure 1 displays the location and starting year for all 138 buoys, superposed with topography

and bathymetry based on ETOPO2 v2 (National Geophysical Data Center, 2006). No potentially biased spatial pattern is apparent in the starting years.

We use the COARE bulk flux algorithm v3.6 (Fairall et al., 2003) to compute LHF (Supplementary Materials S1.2). LHF is defined as positive upward (moisture/heat gain by ARs). Since most buoys do not record dewpoint temperature (T_d), we interpolate hourly near-surface T_d from ERA5 reanalysis on a 0.25°×0.25° grid (Hersbach et al., 2020) to buoy locations by distance-weighting each buoy's surrounding four reanalysis gridpoints. T_d from ERA5 is generally consistent with in situ T_d measurements available from three buoys (Figure S1).

To identify landfalling ARs, we use the SIO-R1, a catalog introduced by Gershunov et al. (2017) applying a new AR detection methodology to the NCEP/NCAR reanalysis (Kalnay et al., 1996). SIO-R1 reports at 6-hourly timesteps (1948–2017) whether regions satisfying AR conditions (≥15 mm total column water vapor (TCWV) and ≥250 kg/m/s vertically integrated vapor transport (IVT), for ≥1,500 km contiguous length) extend across any point along the North American west coast (20–60ºN). At every such timestep, it identifies the location of maximum IVT along the coast, providing IVT and TCWV there. SIO-R1 has been compared to other AR detection algorithms (Ralph et al., 2019b), showing a high level of consistency. We use SIO-R1 from 1979 to 2017 for the overlapping periods of the NDBC buoys and ERA5.

2.2. AR Compositing Procedure

We focus our analysis on strong (lifetime-maximum IVT ≥500 kg/m/s) and late-winter (January–March) ARs. However, Figures S2–S5 show that variations of these criteria (lower vs. higher intensity thresholds, and late vs. whole winters) yield very little changes in results. By selecting stronger ARs (following the threshold of Shinoda et al., 2019), we intend to examine ARs with robust air-sea interaction while ensuring that the analyzed ARs would be detected similarly by alternate catalogs (Ralph et al., 2019b). We select JFM ARs to focus on events occurring when ENSO's influence on coastal SST and west coast precipitation are most robust (Alexander et al., 2002; Capotondi et al., 2019; Chelton & Davis, 1982; Frischknecht et al., 2015; Jong et al., 2016).

SIO-R1 identifies 220 qualifying ARs that impact the U.S. coastline (32.5°–47.5°N) during their lifetime. For each, we determine the lifetime southernmost and northernmost latitude of its maximum IVT location given by SIO-R1. We include data from all buoys in that latitude range (±1° on either side) for composites, averaging buoys within four equal latitudinal bins (4.25º latitude). Composites are centered around each AR's 6-hourly timestep of lifetime maximum IVT and extend 3 days before and after. While AR conditions as defined by a 250 kg/m/s IVT threshold typically last 1–1.5 days at coastal locations, stronger ARs tend to last much longer (Gershunov et al., 2017; Ralph et al., 2013; Rutz et al., 2014). Therefore, our longer compositing window of ±3 days reflects the stringent intensity criteria. Since SIO-R1 provides IVT at only one coastal location per timestep, we must define Day 0 on a coast-wide basis, despite the fact that the maximum IVT might occur at different times along the coast. However, we find no robust shift in the timing of AR conditions with latitude (Figure 2) even though ARs' landfalling location tends to propagate southward along the coast (Figure S6).

For ENSO-phase composites, ARs are composited according to historical El Niño (La Niña) years, defined as when the JFM-averaged Oceanic Niño Index (ONI) exceeds 0.5 (−0.5). Different "flavors" of ENSO, as measured by, for example, the ENSO Longitude Index (Williams & Patricola, 2018), are also known to affect ARs, but via different atmospheric circulation responses (Kim et al., 2019). Furthermore, the mechanism by which noncanonical ENSO modulates coastal SSTs is also likely different and event-dependent (e.g., Capotondi et al., 2019). However, an extended analysis involving different types of ENSO is beyond the scope of the study.
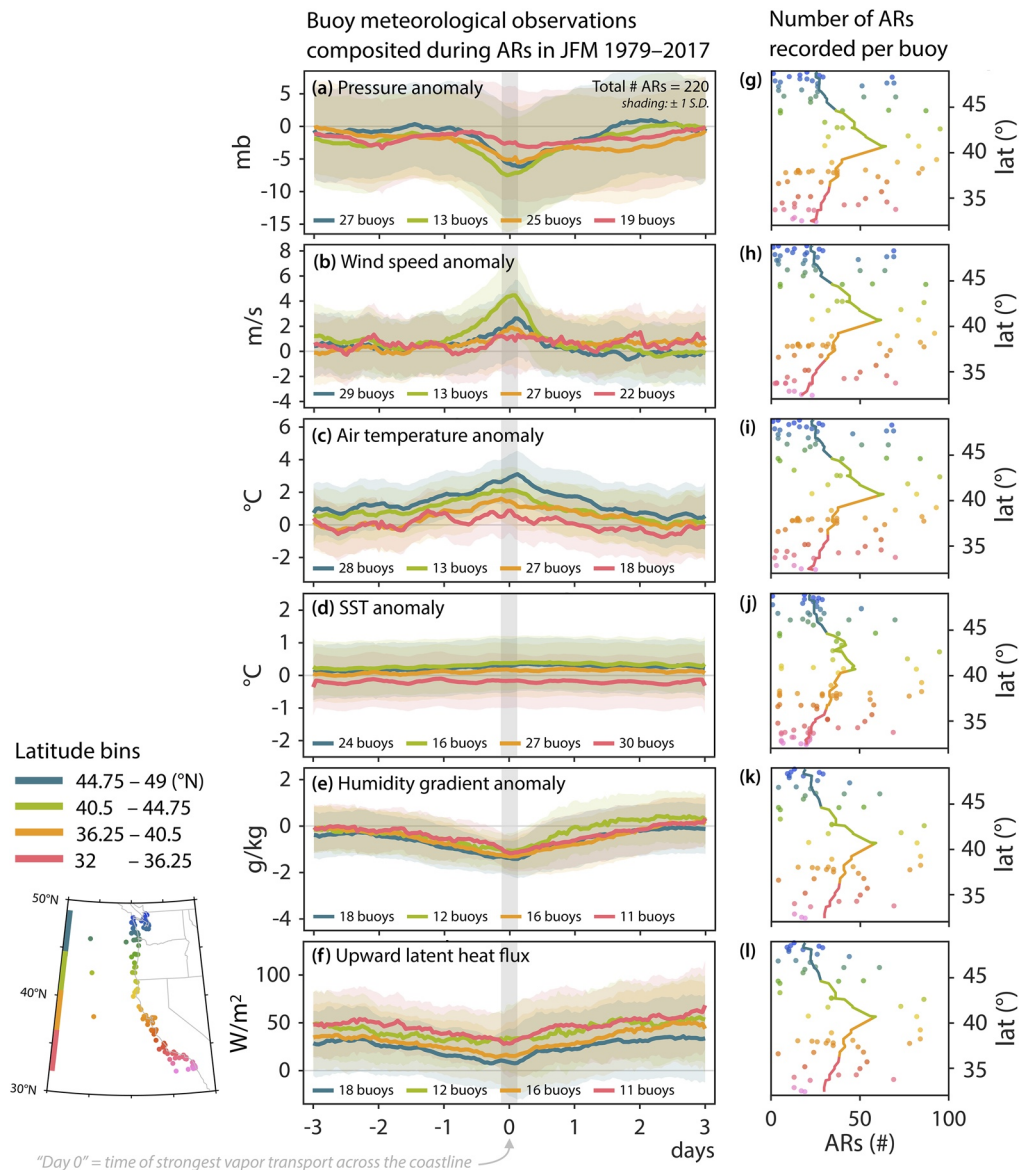
Figure 2. Composite evolution in (a) surface air pressure, (b) wind speed, (c) air temperature, (d) SST, and (e) humidity gradient (all anomalies), and (f) latent heat flux (absolute) during strong late-winter landfalling ARs (1979–2017). Gray vertical shading denotes the time of the ARs' maximum intensity. Colored curves and shading represent latitudinal bin averages and ±1 standard deviation, respectively. The number of buoys contributing to each bin average is also indicated in (a)–(f). (g)–(l): The number of ARs recorded by each buoy (x-axis) for each quantity, plotted against buoy latitudes (y-axis). Line denotes two-degree running average. AR, atmospheric river; SST, sea surface temperature.

3. Results

3.1. All-Year and All-Event Composites

Figure 2 presents composite evolutions of near-surface meteorological quantities from buoys during all strong, late-winter landfalling ARs in 1979–2017, displaying surface pressure, wind speed, air temperature, SST, air-sea humidity gradient (all anomalies), and upward LHF (absolute). AR landfalls (Day 0) are associated with lower pressure, higher wind speed, and warmer and more humid air, and these anomalies extend to ±3 days of landfall. ARs' manifestation in the boundary layer meteorology tends to be most pronounced north of 40.5ºN (Oregon and Washington coasts), while AR frequency peaks around 40.5ºN (southern Oregon and northern California coasts). We find no coherent evolution of nearshore SST during ARs; thus,

LHF evolution is mostly determined by atmospheric variability on synoptic timescales (Section 3.3). On interannual timescales, in contrast, SST variability becomes essential, as discussed in Section 3.2.

Air-sea humidity gradient anomalies dominate the evolution of LHF during synoptic AR events. That is, despite strong winds associated with ARs, LHF typically weakens during peak intensity due to weakly negative humidity gradient anomalies (Shinoda et al., 2019). However, within Day ±1, when LHF is weakest (and LHF anomalies are negative; Figure S7), all latitudinal bin averages of absolute LHF remain positive. Absolute LHF typically ranges from 30–50 W/m^2 throughout total AR lifetimes (southern California, Oregon) or early and late lifetimes (northern California, Washington).

The shading, denoting standard deviation, in Figure 2 indicates substantial event-to-event variability. In particular, during extreme events, LHF may exhibit opposite evolution to the composite mean evolution (Figures 4, S4 & S8). For example, during a landfalling AR in February 2015 with intensity (lifetime-maximum coastal IVT) in the >95th percentile of all ARs in JFM 1979–2017, nearshore LHF was on average 30 W/m^2, with instantaneous estimates exceeding 60 W/m^2, along the central coast (36.25–40.5ºN) (Figure S8, Figure 4). This is in agreement with a similar time-mean LHF for the same AR reported by Shinoda et al. (2019) (their Figures S3 and S5) based on OAFLUX and CALWATER 2015 field measurements (Ralph et al., 2016). Our result adds that LHF estimated from nearshore buoys was similarly high on the southern coast (32–36.25ºN) and often exceeded 100 W/m^2 on the northern coast (40.5–45ºN) (Figure S8).

3.2. ENSO-Phase Composites

Figures 3a–3c show composite evolutions of LHF during landfalling ARs in El Niño and La Niña winters and their difference. LHF during the early and late stages of AR lifetimes (Day >±1) on the southern coast increases by > 30 W/m^2, representing a ≥70% change, from La Niña to El Niño winters (Figure 3c). The northern coast sees an opposite change of similar magnitude, albeit with a weaker late-lifetime difference. This occurs during the portions of AR lifetimes when LHF is typically strongest (Figure 2). During ARs' peak intensity, within Day ±1, when LHF is smallest, the ENSO-related flux differences approach zero.

Figures 3d and 3e show ENSO-associated changes in AR intensity, as measured by IVT and TCWV (from SIO-R1). Generally, AR intensity increases from La Niña to El Niño winters in both metrics. Specifically, intensity increases most strongly before and after ARs' peak intensity (Day >±1), with differences up to ∼90 kg/m/s in IVT and ∼2 mm in TCWV. The increases in AR intensity >±1 day of landfall coincide with the periods when LHF is enhanced along the southern coast (Figures 3a and 3b). These AR intensity composites follow SIO-R1's AR intensity criteria (IVT ≥250 kg/m/s, relaxing our peak-IVT ≥500 kg/m/s criteria) and the period 1950–2017 common between SIO-R1 and ONI. The relaxed threshold and extended period chosen for this analysis maximize the sample sizes of ARs and ENSO years, and underscore the generality of these results (beyond only strong ARs and the temporal limitations imposed by the buoys and ERA5 data). However, our results remain unchanged even if we follow the more restrictive period and threshold (Figure S9).

3.3. Flux Decomposition

We perform a linear decomposition of LHF to estimate contributions from constituent variables, following the procedure by Menezes et al. (2019); (Text S1.2). Figure 4 presents a decomposition of LHF into estimated contributions from surface air stability (S = air temperature minus SST, positive stable), wind speed (U), relative humidity (RH), and SST.

To illustrate how to interpret this result, let us focus first on an extreme AR landfalling near San Francisco on February 5–7, 2015. The black-to-white dots in Figures 4a–4d denote hourly results based on observations from NDBC buoy 46012, located off San Francisco, during this AR (Figure S8). The contributions to LHF (y-axis) were such that the strongest LHF (x-axis) was driven primarily by high wind speed, and partly by SST (note that SST's y-axis is 10× smaller). Meanwhile, stability and humidity mostly suppressed the LHF anomaly, or acted neutrally. While this was one extreme event, its demonstration of canonical AR features,
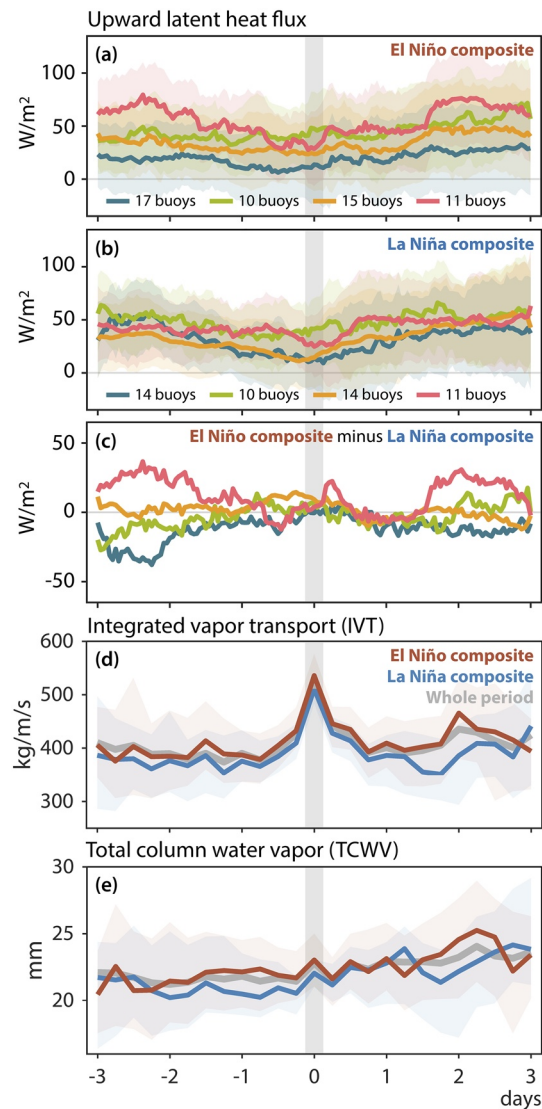
Figure 3. Composite evolutions of absolute latent heat flux during ARs in (a) El Niño and (b) La Niña winters (1979–2017), and (c) El Niño minus La Niña for each latitudinal bin (d)–(e): Composite evolutions of two AR intensity metrics, IVT and TCWV, during ARs in El Niño (red), La Niña (blue), and all (gray) winters (1950–2017). AR, atmospheric river; IVT, integrated vapor transport; TCWV, total column water vapor.

such as strong wind and warm, moist air, lends confidence that the variables' LHF contributions seen here are consistent with ARs of average intensity.

Next, we extend the analysis to the whole late-winter (JFM) of the same year (2015), shown as color-coded scatters in Figures 4a–4d. LHF anomalies were mostly near-zero or weakly negative. Nevertheless, the scattering indicates that strong positive LHF anomalies were primarily caused by high wind speed and dry air, and partly by SST anomalies. Negative LHF anomalies were mainly driven by low wind speed. SST anomalies contributed positively to LHF, likely because 2015 was an El Niño year with anomalously warm SSTs. We also analyzed LHF contributions during only the few ARs affecting this buoy during JFM 2015, with complementary findings emphasizing the role of wind speed and partially SST strengthening LHF (Figure S10).

We also extend this decomposition analysis to all winters (JFM 1979–2017), first focusing only on Buoy 46012 (Figure S11), showing very similar results to the JFM2015 case (Figures 4a–4d) except that SST's contributions are distributed both positively and negatively, as expected due to the inclusion of both El Niño
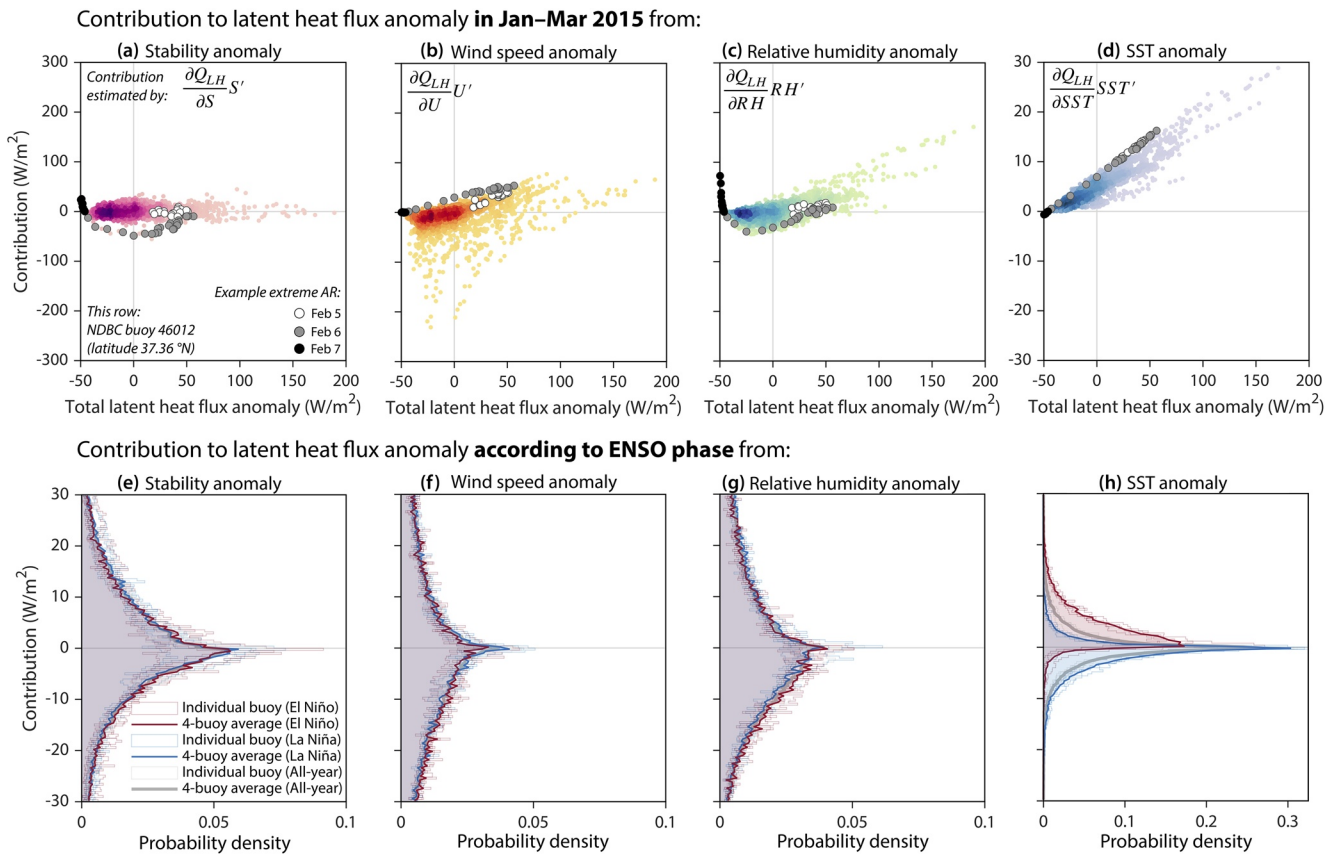
Contribution to latent heat flux anomaly **in Jan–Mar 2015** from:

Contribution to latent heat flux anomaly **according to ENSO phase** from:

Figure 4. (a)–(d): *x*-axis: hourly upward latent heat flux (LHF) anomaly at NDBC buoy 46012 for January–March (JFM) 2015. *Y*-axis: contribution to that LHF anomaly from (a) air-sea stability, (b) wind speed, (c) relative humidity, and (d) SST anomalies. Color intensity indicates dot density. White-to-black dots denote 5–7 February during an extreme AR. *Note.* the smaller *y*-scale for SST (d). (e)–(h): Distributions of LHF contributions are shown along the *y*-axis for El Niño JFM (red), La Niña JFM (blue), and all JFM (gray) in 1979–2017. Pale lines show individual histograms for four buoys along the coast; dark lines show average distributions across all four buoys. *Note.* the larger *x*-scale for SST (h). AR, atmospheric river; NDBC, National Data Buoyancy Center; SST, sea surface temperature.

and La Niña winters. In Figures 4e–4h, for four buoys spanning the coast, we present probability distributions of contributions from each variable to LHF separately during El Niño winters, La Niña winters, and all winters. Whereas LHF contribution distributions from stability, wind speed, and relative humidity are apparently independent of the ENSO phases, SST's contribution distribution clearly varies with the ENSO phases. Figures S12–S13 show the same results for each of the buoys separately.

4. Discussion

Our composite analyses of buoy-based LHF show that strong late-winter ARs landfalling along the U.S. west coast typically receive strong upward absolute LHF (30–50 W/m^2) 1–3 days before and after their landfalls. In contrast, during landfall (Day $<\pm1$), LHF reaches its minimum (Figure 2). El Niño winters are associated with increased LHF along the southern coast and decreased LHF along the northern coast, while opposite changes occur during La Niña. Enhanced southern-coastal LHF during El Niño corresponds with generally intensified ARs (Figure 3). LHF decomposition revealed that during an El Niño winter at a buoy near San Francisco, strong LHF was primarily driven by high wind speed and dry air, while SST contributions were smaller but almost exclusively positive. These results raise several discussion points concerning the relationship between nearshore SST, LHF, and AR intensity.

First, the all-year and all-event composites show that nearshore LHF evolution during landfalling ARs primarily reflects the near-surface humidity gradient. However, although the evolutions of humidity gradient anomaly are almost identical between the different latitudinal bins, the evolutions of absolute LHF are not, likely due to latitudinal variations in background SST. That is, the LHF is strongest along the southern coast, where

SST is warmer, even though the air is also warmer and moister. Latitudinal variations in background SST are therefore a primary factor influencing the LHF experienced by landfalling ARs on synoptic time-scales.

How, then, may temporal variations in background SST, mainly driven by ENSO on interannual timescales, contribute to LHF variations during ARs? We found that along the entire coast, and not necessarily limited to AR conditions, SST anomalies strengthen LHF during El Niño winters and weaken it during La Niña. In contrast, the effects of relative humidity, wind speed, and near-surface stability on LHF remain mostly unchanged between ENSO phases (Figure 4, S12, S13). Therefore, we propose that, while other variables drive nearshore LHF variations on synoptic timescales, ENSO-induced SST variations are the primary contributor to interannual variations in AR-associated LHF. However, SST anomalies' effect on LHF may be limited along the northern coast, where LHF tends to be weaker during El Niño ARs despite warm SST anomalies (Figures 3c and 4h).

Finally, Figure 3 suggests a potential relationship between nearshore LHF and AR intensity. ARs typically intensify during El Niño winters along the southern coast. The midlatitude storm track shifts southward during El Niño (Seager et al., 2010; Trenberth et al., 1998), with average ARs landfalling latitude also shifting southward (Figure S6; Payne & Magnusdottir, 2014). Since we find that nearshore LHF increases during El Niño along the southern coast, the intensified ARs in El Niño winters would experience both climatologically stronger (due to latitude) and anomalously enhanced (due to ENSO) LHF during landfall. Recent studies emphasize that large-scale circulation changes over the Pacific enhance onshore IVT during El Niño, intensifying southwestern U.S. precipitation (Guirguis et al., 2018; Kim & Alexander, 2015; Kim et al., 2019). Our results suggest that the local contribution from enhanced nearshore LHF may also play a role in intensifying ARs during El Niño (Chen & Leung, 2020).

Persson et al. (2005) observed that nearshore turbulent heat fluxes in southern California significantly destabilized boundary layer air in a landfalling AR. From offshore LHF of 32 W/m^2 derived from field measurements, they estimated boundary-layer convective available potential energy (CAPE) to be enhanced by 26% as the AR approached the shore, proposing that nearshore SST anomalies during El Niño had likely enabled this effect. Our results support this by demonstrating covariability between nearshore SST, LHF, and landfalling AR intensity during El Niño. Furthermore, while Persson et al. (2005)'s study was limited to a single AR during an El Niño year at southern latitude, we observe that absolute LHF typically exceeds 30 W/m^2 throughout all or some of AR lifetimes at all coastal latitudes (Figures 3a–3c), implying that the conditions for such an effect of coastal LHF on ARs may occur more generally, extending to northern latitudes and non-El Niño years.

5. Conclusions

This study characterizes nearshore air-sea interaction during landfalling ARs by making use of 138 over-shelf buoys to observe coastal meteorology and SST along the U.S. west coast. Collectively, these moored observations enable a systematic synoptic-scale analysis of a multidecadal (39-year) record of ARs through their high spatial (alongshore) density and fine temporal resolution. Because the buoys are mostly moored over the continental shelf, with typical coastal proximities under 30 km, they can offer a unique view of coastal air-sea processes at the time of AR landfall.

Late-winter ARs experience upward LHF throughout their 6-day landfalling lifetimes, despite LHF weakening within ±1 day of events' peak intensity. LHF typically exceeds 30 W/m^2 throughout partial or total AR lifetimes and is strongest at southernmost and weakest at northernmost latitudes. As indicated in a case study by Persson et al. (2005), nearshore LHF of such magnitudes may be sufficient to destabilize the nearshore boundary layer air, potentially intensifying subsequent precipitation. With our extended period and region examined, we demonstrate that such interaction between ARs and the coastal ocean through LHF may be more ubiquitous.

During El Niño winters along the southern coast, nearshore LHF increases by ∼30 W/m^2 (>70%) from La Niña winters, during ±1–3 days from ARs' peak intensity. Opposite changes occur along the northern coast. The enhanced LHF along the southern coast early and late in AR landfalling lifetimes coincides with inten-

sified ARs during El Niño. AR intensification is most strongly manifested early and late in their landfalling lifetimes, though it is ostensible throughout (Figures 3d and 3e).

Finally, flux decomposition demonstrates that LHF is primarily controlled by wind speed, relative humidity, and stability on synoptic to seasonal timescales. However, on interannual timescales, SST anomalies modulated by ENSO dominantly control the variations in LHF experienced by ARs between different ENSO phases.

Data Availability Statement

Buoy data available at https://bit.ly/3g4LByx, SIO-R1 at https://bit.ly/2CS15aE, and ERA5 at https://bit.ly/2X3HivE.

References

Alexander, M. A., Bladé, I., Newman, M., Lanzante, J. R., Lau, N.-C., & Scott, J. D. (2002). The atmospheric bridge: The influence of ENSO teleconnections on air–sea interaction over the global oceans. *Journal of Climate*, *15*(16), 2205–2231. https://doi.org/10.1175/1520-0442(2002)015%3C2205:TABTIO%3E2.0.CO;2

Algarra, I., Nieto, R., Ramos, A. M., Eiras-Barca, J., Trigo, R. M., & Gimeno, L. (2020). Significant increase of global anomalous moisture uptake feeding landfalling Atmospheric Rivers. *Nature Communications*, *11*, (1), http://dx.doi.org/10.1038/s41467-020-18876-w

Capotondi, A., Sardeshmukh, P. D., Di Lorenzo, E., Subramanian, A. C., & Miller, A. J. (2019). Predictability of US west coast ocean temperatures is not solely due to ENSO. *Scientific Reports*, *9*(1), 10993. https://doi.org/10.1038/s41598-019-47400-4

Chelton, D. B., & Davis, RÍ. E. (1982). Monthly mean sea-level variability along the west coast of North America. *Journal of Physical Oceanography*, *12*(8), 757–784. https://doi.org/10.1175/1520-0485(1982)012<0757:MMSLVA>2.0.CO;2

Chen, X., & Leung, L. R. (2020). Response of landfalling atmospheric rivers on the U.S. west coast to local sea surface temperature perturbations. *Geophysical Research Letters*, *47*(18).e2020GL089254. https://doi.org/10.1029/2020GL089254

Cronin, M. F., Gentemann, C. L., Edson, J., Ueki, I., Bourassa, M., Brown, S., et al. (2019). Air-Sea Fluxes With a Focus on Heat and Momentum. *Frontiers in Marine Science*, *6*, https://doi.org/10.3389/fmars.2019.00430

Corringham, T. W., Ralph, F. M., GershunovCayan, A. D. R., & Talbot, C. A. (2019). Atmospheric rivers drive flood damages in the western United States. *Science Advances*, *5*, 1–7. https://doi.org/10.1126/sciadv.aax4631

Dettinger, M., & Coauthors (2012). Design and quantification of an extreme winter storm scenario for emergency preparedness and planning exercises in California. *Natural Hazards*, *60*, 1085–1111. https://doi.org/10.1007/s11069-011-9894-5

Dettinger, M. D. (2013). Atmospheric rivers as drought busters on the U.S. west coast. *Journal of Hydrometeorology*, *14*(6), 1721–1732. https://doi.org/10.1175/JHM-D-13-02.1

Dettinger, M. D., Ralph, F. M., Das, T., Neiman, P. J., & Cayan, D. R. (2011). Atmospheric rivers, floods and the water resources of California. *Water*, *3*(2), 445–478. https://doi.org/10.3390/w3020445

Fairall, C. W., Bradley, E. F., Hare, J. E., Grachev, A. A., & Edson, J. B. (2003). Bulk parameterization of air–sea fluxes: Updates and verification for the COARE algorithm. *Journal of Climate*, *16*(4), 571–591. https://doi.org/10.1175/1520-0442(2003)016<0571:BPOASF>2.0.CO;2

Frischknecht, M., Münnich, M., & Gruber, N. (2015). Remote versus local influence of ENSO on the California Current System. *Journal of Geophysical Research: Oceans*, *120*(2), 1353–1374. https://doi.org/10.1002/2014JC010531

Gershunov, A., Shulgina, T., Ralph, F. M., Lavers, D. A., & Rutz, J. J. (2017). Assessing the climate-scale variability of atmospheric rivers affecting western North America. *Geophysical Research Letters*, *44*, 7900–7908. https://doi.org/10.1002/2017GL074175

Gonzales, K. R., Swain, D. L., Nardi, K. M., Barnes, E. A., & Diffenbaugh, N. S. (2019). Recent warming of landfalling atmospheric rivers along the west coast of the United States. *Journal of Geophysical Research: Atmosphere*, *124*(13), 6810–6826. https://doi.org/10.1029/2018JD029860

Guan, B., Molotch, N. P., Waliser, D. E., Fetzer, E. J., & Neiman, P. J. (2010). Extreme snowfall events linked to atmospheric rivers and surface air temperature via satellite measurements. *Geophysical Research Letters*, *37*(20), L20401. https://doi.org/10.1029/2010GL044696

Guirguis, K., Gershunov, A., Clemesha, R. E. S., Shulgina, T., Subramanian, A. C., & Ralph, F. M. (2018). Circulation drivers of atmospheric rivers at the North American west coast. *Geophysical Research Letters*, *45*(22), 12576–12584. https://doi.org/10.1029/2018GL079249

Hersbach, H., Bell, B., Berrisford, P., Hirahara, S., Horányi, A., Muñoz-Sabater, J., et al. (2020). The ERA5 global reanalysis. *Quarterly Journal of the Royal Meteorological Society*, *146*(730), 1999–2049. https://doi.org/10.1002/qj.3803

Jong, B.-T., Ting, M., & Seager, R. (2016). El Niño's impact on California precipitation: seasonality, regionality, and El Niño intensity. *Environmental Research Letters*, *11*(5).054021. https://doi.org/10.1088/1748-9326/11/5/054021

Kalnay, E., & Co-authors (1996). The NCEP/NCAR 40-Year Reanalysis Project. *Bulletin of American Meteorological Society*, *77*, 437–471. https://doi.org/10.1175/1520-0477(1996)077<0437:TNYRP>2.0.CO;2

Kim, H.-M., & Alexander, M. A. (2015). ENSO's modulation of water vapor transport over the Pacific–North American Region. *Journal of Climate*, *28*(9), 3846–3856. https://doi.org/10.1175/JCLI-D-14-00725.1

Kim, H.-M., Zhou, Y., & Alexander, M. A. (2019). Changes in atmospheric rivers and moisture transport over the Northeast Pacific and western North America in response to ENSO diversity. *Climate Dynamics*, *52*(12), 7375–7388. https://doi.org/10.1007/s00382-017-3598-9

Lavers, D. A., Allan, R. P., Wood, E. F., Villarini, G., Brayshaw, D. J., & Wade, A. J. (2011). Winter floods in Britain are connected to atmospheric rivers. *Geophysical Research Letters*, *38*, L23803. https://doi.org/10.1029/2011GL049783

Leung, L. R., & Qian, Y. (2009). Atmospheric rivers induced heavy precipitation and flooding in the western U.S. simulated by the WRF regional climate model. *Geophysical Research Letters*, *36*, L03820. https://doi.org/10.1029/2008GL036445

Menezes, V. V., Farrar, J. T., & Bower, A. S. (2019). Evaporative implications of dry-air outbreaks over the northern Red Sea. *Journal of Geophysical Research: Atmosphere*, *124*(9), 4829–4861. https://doi.org/10.1029/2018JD028853

Moore, B. J., Neiman, P. J., Ralph, F. M., & Barthold, F. E. (2012). Physical processes associated with heavy flooding rainfall in Nashville, Tennessee, and vicinity during 1–2 May 2010: The role of an atmospheric river and mesoscale convective systems. *Monthly Weather Review*, *140*, 358–378. https://doi.org/10.1175/MWR-D-11-00126.1

Neiman, P. J., Ralph, F. M., Wick, G. A., Kuo, Y.-H., Wee, T.-K., Ma, Z., et al. (2008). Diagnosis of an intense atmospheric river impacting the Pacific Northwest: Storm summary and offshore vertical structure observed with COSMIC satellite retrievals. *Monthly Weather Review*, *136*, 4398–4420. https://doi.org/10.1175/2008MWR2550.1

Neiman, P. J., Schick, L. J., Ralph, F. M., Hughes, M., & Wick, G. A. (2011). Flooding in Western Washington: The connection to atmospheric rivers. *Journal of Hydrometeorology*, *12*(6), 1337–1358. https://doi.org/10.1175/2011JHM1358.1

Payne, A. E., & Magnusdottir, G. (2014). Dynamics of landfalling atmospheric rivers over the north Pacific in 30 Years of MERRA reanalysis. *Journal of Climate*, *27*(18), 7133–7150. https://doi.org/10.1175/JCLI-D-14-00034.1

Persson, P. O. G., Neiman, P. J., Walter, B., Bao, J.-W., & Ralph, F. M. (2005). Contributions from California Coastal-Zone surface fluxes to heavy coastal precipitation: A CALJET case study during the strong El Niño of 1998. *Monthly Weather Review*, *133*(5), 1175–1198. https://doi.org/10.1175/MWR2910.1

Ralph, F. M., Coleman, T., Neiman, P. J., Zamora, R. J., & Dettinger, M. D. (2013). Observed Impacts of duration and seasonality of atmospheric-river landfalls on soil moisture and runoff in coastal Northern California. *Journal of Hydrometeorology*, *14*(2), 443–459. https://doi.org/10.1175/JHM-D-12-076.1

Ralph, F. M., & Dettinger, M. D. (2012). Historical and national perspectives on extreme West Coast precipitation associated with atmospheric rivers during December 2010. *Bulletin of the American Meteorological Society*, *93*, 783–790. https://doi.org/10.1175/BAMS-D-11-00188.1

Ralph, F. M., Neiman, P. J., Kiladis, G. N., Weickman, K., & Reynolds, D. W. (2011). A multi-scale observational case study of a Pacific atmospheric river exhibiting tropical–extratropical connections and a mesoscale frontal wave. *Monthly Weather Review*, *139*, 1169–1189. https://doi.org/10.1175/2010MWR3596.1

Ralph, F. M., Neiman, P. J., & Rotunno, R. (2005). Dropsonde observations in low-level jets over the northeastern Pacific Ocean from CALJET-1998 and PACJET-2001: Mean vertical-profile and atmospheric-river characteristics. *Monthly Weather Review*, *133*(4), 889–910. https://doi.org/10.1175/MWR2896.1

Ralph, F. M., Neiman, P. J., Wick, G. A., Gutman, S. I., Dettinger, M. D., Cayan, D. R., & White, A. B. (2006). Flooding on California's Russian River: Role of atmospheric rivers. *Geophysical Research Letters*, *33*, L13801. https://doi.org/10.1029/2006GL026689

Ralph, F. M., Neiman, P. J., & Wick, G. A. (2004). Satellite and CALJET aircraft observations of atmospheric rivers over the eastern north Pacific Ocean during the winter of 1997/98. *Monthly Weather Review*, *132*(7), 1721–1745. https://doi.org/10.1175/1520-0493(2004)132<1721:SACAOO>2.0.CO;2

Ralph, F. M., Prather, K. A., Cayan, D., Spackman, J. R., DeMott, P., Dettinger, M., et al. (2016). CalWater field studies designed to quantify the roles of atmospheric rivers and aerosols in modulating u.s. west coast precipitation in a changing climate. *Bulletin of the American Meteorological Society*, *97*(7), 1209–1228. https://doi.org/10.1175/BAMS-D-14-00043.1

Ralph, F. M., Rutz, J. J., Cordeira, J. M., Dettinger, M., Anderson, M., Reynolds, D., et al. (2019a). A scale to characterize the strength and impacts of atmospheric rivers. *Bulletin of the American Meteorological Society*, *100*, 269–289. https://doi.org/10.1175/BAMS-D-18-0023.1

Ralph, F. M., Wilson, A. M., Shulgina, T., Kawzenuk, B., Sellars, S., Rutz, J. J., et al. (2019b). ARTMIP-early start comparison of atmospheric river detection tools: How many atmospheric rivers hit northern California's Russian River watershed? *Climate Dynamics*, *52*(7), 4973–4994. https://doi.org/10.1007/s00382-018-4427-5

Rutz, J. J., Steenburgh, W. J., & Ralph, F. M. (2014). Climatological characteristics of atmospheric rivers and their inland penetration over the western United States. *Monthly Weather Review*, *142*(2), 905–921. https://doi.org/10.1175/MWR-D-13-00168.1

Seager, R., Kushnir, Y., Nakamura, J., Ting, M., & Naik, N. (2010). Northern Hemisphere winter snow anomalies: ENSO, NAO and the winter of 2009/10. *Geophysical Research Letters*, *37*(14), L14703. https://doi.org/10.1029/2010GL043830

Shinoda, T., Zamudio, L., Guo, Y., Metzger, E. J., & Fairall, C. W. (2019). Ocean variability and air-sea fluxes produced by atmospheric rivers. *Scientific Reports*, *9*(1), 2152. https://doi.org/10.1038/s41598-019-38562-2

Smith, B. L., Yuter, S. E., Neiman, P. J., & Kingsmill, D. E. (2010). Water vapor fluxes and orographic precipitation over northern California associated with a land-falling atmospheric river. *Monthly Weather Review*, *138*, 74–100. https://doi.org/10.1175/2009MWR2939.1

Todd, R. E., Rudnick, D. L., Davis, R. E., & Ohman, M. D. (2011). Underwater gliders reveal rapid arrival of El Niño effects off California's coast. *Geophysical Research Letters*, *38*(3), L03609. https://doi.org/10.1029/2010GL046376

Trenberth, K. E., Branstator, G. W., Karoly, D., Kumar, A., Lau, N.-C., & Ropelewski, C. (1998). Progress during TOGA in understanding and modeling global teleconnections associated with tropical sea surface temperatures. *Journal of Geophysical Research: Oceans*, *103*, 14291–14324. https://doi.org/10.1029/97JC01444

White, A. B., & Coauthors (2012). NOAA's rapid response to the Howard A. Hanson Dam flood risk management crisis. *Bulletin of the American Meteorological Society*, *93*, 189–207. https://doi.org/10.1175/BAMS-D-11-00103.1

Williams, I. N., & Patricola, C. M. (2018). Diversity of ENSO events unified by convective threshold sea surface temperature: A nonlinear ENSO index. *Geophysical Research Letters*, *45*(17), 9236–9244. https://doi.org/10.1175/BAMS-D-11-00103.1

Yu, L., & Weller, R. A. (2007). Objectively analyzed air–sea heat fluxes for the global ice-free oceans (1981–2005). *Bulletin of the American Meteorological Society*, *88*(4), 527–540. https://doi.org/10.1175/BAMS-88-4-527

Zhang, Z., Ralph, F. M., & Zheng, M. (2019). The relationship between extratropical cyclone strength and atmospheric river intensity and position. *Geophysical Research Letters*, *46*, 1814–1823. https://doi.org/10.1029/2018GL079071

Zhu, Y., & Newell, R. E. (1998). A proposed algorithm for moisture fluxes from atmospheric rivers. *Monthly Weather Review*, *126*(3), 725–735. https://doi.org/10.1175/1520-0493(1998)126<0725:APAFMF>2.0.CO;2

References From the Supporting Information

Bosilovich, M. G., Robertson, F. R., Takacs, L., Molod, A., & Mocko, D. (2017). Atmospheric water balance and variability in the MERRA-2 reanalysis. *Journal of Climate*, *30*(4), 1177–1196. https://doi.org/10.1175/JCLI-D-16-0338.1

Emanuel, K. A. (1994). *Atmospheric convection*. Oxford University Press. Retrieved from https://rmets.onlinelibrary.wiley.com/doi/10.1002/joc.3370150710

Richter, I., & Xie, S.-P. (2008). Muted precipitation increase in global warming simulations: A surface evaporation perspective. *Journal of Geophysical Research: Atmosphere*, *113*, D24118. https://doi.org/10.1029/2008JD010561

Vimont, D. J., Alexander, M., & Fontaine, A. (2009). Midlatitude excitation of tropical variability in the Pacific: The role of thermodynamic coupling and seasonality. *Journal of Climate*, *22*(3), 518–534. https://doi.org/10.1175/2008JCLI2220.1